

Smart Skins Based on Assembled Piezoresistive Networks of Sustainable Graphene Microcapsules for High Precision Health Diagnostics

Adel K. A. Aljarid, Ming Dong, Yi Hu, Cencen Wei, Jonathan P. Salvage, Dimitrios G. Papageorgiou,* and Conor S. Boland*

The environmental impact of plastic waste has had a profound effect on our livelihoods and there is a need for future plastic-based epidermal electronics to trend toward more sustainable approaches. Infusing graphene into the culinary process of seaweed spherification produces core-shell, food-based nanocomposites with properties exhibiting a remarkably high degree of tunability. Unusually, mechanical, electrical, and electromechanical metrics all became decoupled from one another, allowing for each to be individually tuned. This leads to the formation of a general electromechanical model which presents a universal electronic blueprint for enhanced performances. Through this model, performance optimization and system miniaturization are enabled, with gauge factors (G) >108 for capsule diameters (D) $\approx 290 \mu\text{m}$ and produced at a record rate of >100 samples per second. When coalesced into quasi-2D planar networks, microcapsules form the basis of discrete, recyclable electronic smart skins with areal independent sensitivities for muscular, breathing, pulse, and blood pressure measurements in real-time.

duce flexible, electromechanically sensitive materials for mechanical strain sensing.^[3,4] The utility of these materials lies in their ability to potentially facilitate the creation of smart wearable skin-on devices for high precision, real-time biomechanical and vital signs measurements.^[5,6] Past research on utilizing the electromechanical response of graphene networks has demonstrated composite materials in many forms; from mixed-phase solid films,^[7-9] foams,^[10-12] fibers,^[13,14] fabrics,^[15-17] gels,^[18-20] to microstructured^[21-23] and templated^[17,24,25] heterostructures. The popularity of applying graphene nanocomposites lay in the cost efficiency associated with making nanosheets in the liquid phase and the cheap polymer materials applied to fabricate devices.

However, most methodologies apply solvent systems and polymer materials that in the future could be damaging to the environment and human health if or when they require disposal.^[26]

Furthermore, there is a need to develop devices that better meet the requirements for healthcare applications, with very few materials presenting the desired combination of high sensitivity and low mechanical stiffnesses that are required to measure minute bodily signals like heart function accurately and unimpeded.^[3] Many of these issues arise from filler network, mechanical and electromechanical properties of materials being coupled to one another. As such, if these properties could be decoupled, the mechanisms in which performances may be controlled or improved would be unlocked.

Here, we added graphene to brown seaweed derivatives through a process known as spherification,^[27] a molecular gastronomy method used to create edible, biodegradable capsules containing liquified food products. In the food and hospitality industries, these materials are known as food caviar.^[28] Applying a modified version of this method, graphene could be incorporated into the capsule procedure to make graphene-seaweed nanocomposite capsules at a record rate of >100 samples per second. Expectedly, the presence of graphene increased the system's electrical conductivity; however, unlike other nanocomposite systems,^[2] graphene loadings and alignment had no effect on mechanical properties. Resulting in extremely soft materials. During mechanical deformation, capsules displayed a large


1. Introduction

Adding graphene to polymers to create electronic textiles has been one of the research pillars of materials science for many decades.^[1,2] Of particular interest are the creation of soft graphene nanocomposites based on elasticated matrices to pro-

A. K. A. Aljarid, C. Wei, C. S. Boland
School of Mathematical and Physical Sciences
University of Sussex
Brighton BN1 9QH, UK
E-mail: c.s.boland@sussex.ac.uk

M. Dong, Y. Hu, D. G. Papageorgiou
School of Engineering and Materials Science
Queen Mary University
London E1 4NS, UK
E-mail: d.papageorgiou@qmul.ac.uk

J. P. Salvage
School of Pharmacy and Biomolecular Sciences
University of Brighton
Brighton BN2 4GJ, UK

 The ORCID identification number(s) for the author(s) of this article can be found under <https://doi.org/10.1002/adfm.202303837>

DOI: 10.1002/adfm.202303837

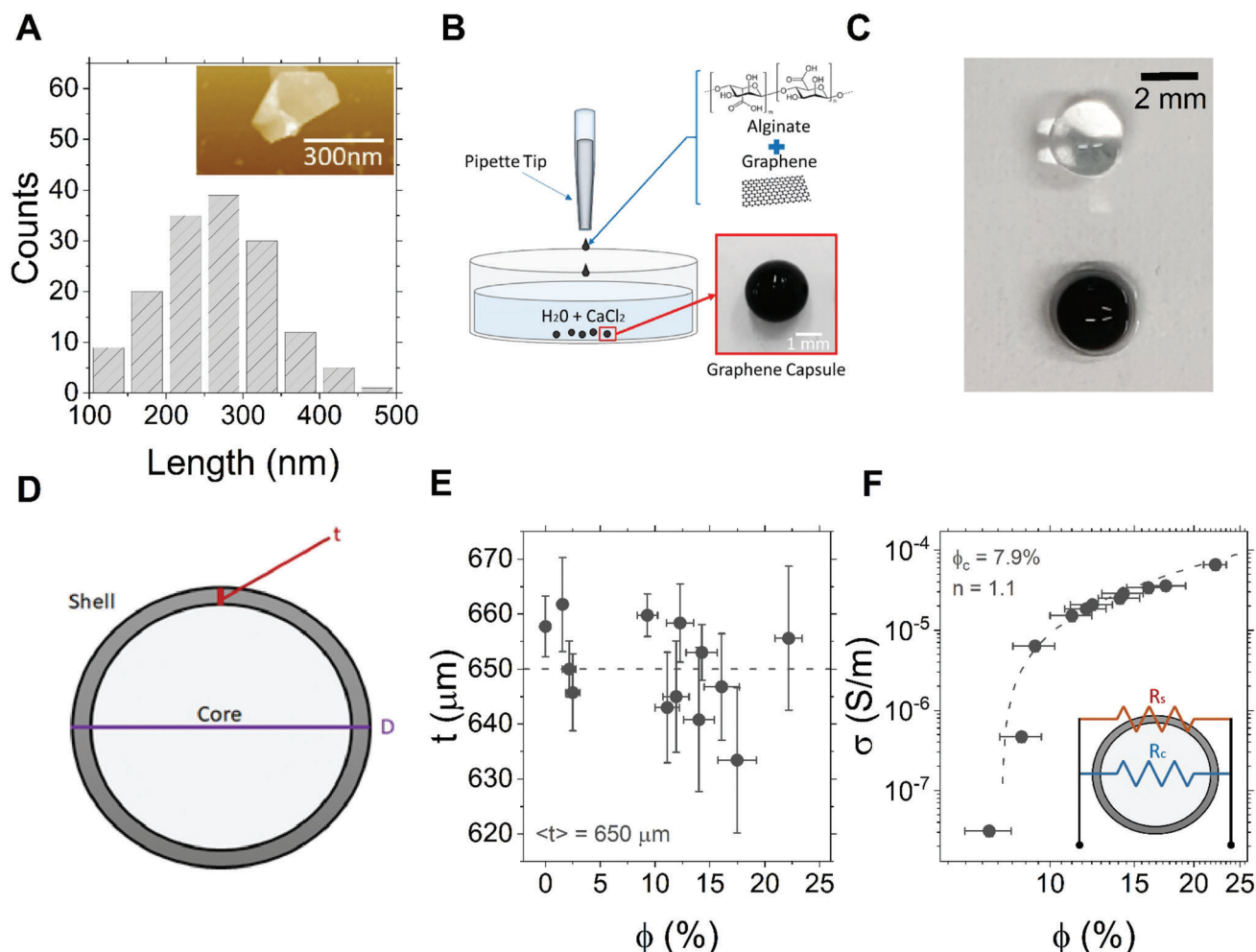


Figure 1. Basic Capsule Properties. A) Histogram of graphene nanosheet length from Atomic Force Microscopy, (inset) representative nanosheet. B) Scheme of graphene capsule production through drop-by-drop method using a pipette. Aqueous dispersion of graphene is premixed with alginate and dispensed into a curing bath of CaCl_2 . C) Photograph of pristine capsule (top) and 9.3 volume% graphene capsule (bottom). D) Diagram showing the structure of a graphene capsule of diameter D is composed of a hydrogel shell of thickness t consisting of graphene nanosheets impeded in a cross-linked calcium alginate polymer matrix and a liquid graphene suspension core. E) Thickness of the hydrogel shell versus shell graphene volume%. Dashed line represents mean thickness value of $650 \mu\text{m}$. F) Shell electrical conductivity as a function of shell graphene volume%. Dashed lines are a fit of Equation 1 with fit parameters of percolation threshold $\phi_c \approx 7.9\%$ percolation constant $n \approx 1.1$. Insert is a circuit diagram of a graphene capsule where R_s and R_c are the shell and core resistances respectively.

electromechanical response that was easily controlled by geometric composition, allowing for the decoupling of performance metrics. Through our developed general electromechanical model, our sustainable capsules could be optimized, and their size scaled towards micron level to create quasi-2D microcapsule networks with areal independent properties that formed the basis of discrete smart skins for high sensitivity bodily sensing. Furthermore, due to our electronic skin's unique heterostructure, we demonstrate a device which has the capability of recycling less sustainable materials associated with their assembly.

2. Results and Discussion

2.1. Characterization of Graphene Capsules

Graphene nanosheet suspensions used in the study were prepared through the liquid phase exfoliation of graphite in an aqueous surfactant solution,^[29] with nanosheets noted to be $\approx 290 \text{ nm}$ in length (Figure 1A), 1–6 layers thick^[30] and defect free (Figure S1, Supporting Information). Sodium alginate was then mixed into the graphene suspensions and the subsequent mixed phase blend extruded into a curing bath of calcium chloride/water, drop-by-drop via a handheld pipette (Figure 1B). Upon contact with the bath, droplets of graphene dispersion formed a gelled coating, creating free-standing spherical materials $\approx 2.5 \text{ mm}$ in diameter (D), which we called capsules, that sunk to the bottom of the bath (Figure S2, Supporting Informa-

tion). Specifically, alginate is a family of unbranched polymers composed of 1,4-linked β -D-mannuronic and α -L-guluronic acid. During capsule formation, Ca^{2+} cations formed from the dissociation of the calcium chloride salt in the water bath interact ionically with blocks of guluronic acid. This mechanism results in the formation of a gelled network described by the “egg-box” structural model.^[31] To note, the methodology detailed here in theory could be applied to a broad range on nanofiller types (i.e., other nanosheet variants or 1D materials like nanotubes or rods) if such materials were to be stabilized in aqueous media to form inks. This allows for the potential tuning of capsule properties based on nanofiller aspect ratio.^[32]

In comparison to the transparent pristine capsules, graphene capsules had an opaque dark hue (Figure 1C). The basic structure of the capsules was described in Figure 1D, where a graphene/alginate hydrogel shell was shown to encapsulate a volume of graphene suspension, forming a core-shell system. Through Scanning Electron Microscopy in Figure S3 (Supporting Information), both the pristine and graphene loaded shells presented smooth, uniform, featureless surfaces. We note that during the formation of the capsules, all alginate migrated to the surface of the droplet to form the shell, leaving no noticeable trace of the polymer in the capsule’s liquid core (Figure S4, Supporting Information). For the shell thickness (t) measured via profilometry (Figure S5, Supporting Information) in Figure 1E, it was found to be ≈ 650 μm irrespective of the shell’s graphene volume%, which was calculated through Thermogravimetric Analysis in Figure S6 (Supporting Information). However, in Figure 1F, we note the electrical conductivity (κ) of the capsules increased from $\approx 10^{-7}$ S m^{-1} at 7.9 volume% of graphene in the shell to $\approx 10^{-4}$ S m^{-1} for 22.1 volume%, which is consistent with percolation-like scaling^[33] described by the following:

$$\kappa \propto (\phi - \phi_c)^n \quad (1)$$

where ϕ , ϕ_c , and n are the shell’s graphene volume%, the percolation threshold and, the percolation exponent, respectively. Cromulent fit parameters of $\phi_c \approx 7.9$ volume% and $n \approx 1.1$ for Equation 1 were found to overlay the data well in the Figure 1F.^[34] The value for the percolation exponent here was consistent with 2D transport, implying current flowed only through the shell. An inset in Figure 1F shows a circuit diagram which describes charge transport through the capsule system. Here, the resistance associated with transport via the liquid core (R_C) far exceeds that of the graphene filled shell resistance (R_S). This resulted in charge transport through the shell being the dominant mechanism and our measurement of κ a description of transport through the shell.

2.2. Mechanical and Electromechanical Properties

In Figure 2A, we show a scheme of our experimental setup which facilitated both mechanical and electromechanical data describing our capsules to be recorded simultaneously. When deformed via mechanical compression, capsule mechanical properties were observed to be decoupled from shell graphene volume% in Figures S7 and S8 (Supporting Information). We believe this invariance was due to poor interfacial interactions

between the hydrophobic graphene filler and hydrophilic alginate matrix that was highlighted by an invariant glass transition temperature measured using Differential Scanning Calorimetry (Figure S9, Supporting Information). Similar behavior was seen previously in hydrogel films based on a graphene/alginate mixture.^[35] Specifically, Young’s modulus (Y) in Figure 2B had an extremely low mean value of ≈ 8.9 Pa across all shell loadings, making our nanocomposites one of the softest on record. On average, strain sensing nanocomposites report $Y \approx 300$ MPa, far above the usable limit of $Y < 300$ kPa for health sensing applications.^[3]

We also observed that while undergoing compressive strain ($-\epsilon$) the electrical resistance of our capsules began to increase, making these materials potential strain sensors. The general mechanism we propose for this resistive electromechanical response in a nanocomposite material was described in Figure 2C and is based on Simmons description of junction resistance.^[36] Initially, at low strain, resistance will increase linearly as the areal overlap (A) of the graphene nanosheets decreases due to divergence with strain. At an intrinsic critical strain, nanosheets will no longer overlap one another and the hopping distance (d) between nanosheets will begin to change, generally resulting in an exponential increase in resistance. Looking at electromechanical response in terms of a fractional resistance ($\Delta R/R_0$) change, the slope of the initial linear increase in $\Delta R/R_0$ can be described using the following:

$$\frac{\Delta R}{R_0} = G\epsilon \quad (2)$$

Where G is the sensitivity metric, the gauge factor.^[20] The absolute strain value at which $\Delta R/R_0$ begins to exponentially change and the fit for Equation 2 fails is known as the working factor (W) metric and is believed to be related to the yield strain at low filler loadings.^[3]

Looking at the electromechanical response of our capsules in Figure 2D and Figure S10 (Supporting Information), we note two distinctive regions in our $\Delta R/R_0$ versus $-\epsilon$ curves: a linear increase in $\Delta R/R_0$ until a critical strain, followed by an exponential decrease. This exponential decrease is a common feature in compressive strain sensors and is an unremarkable combination of geometric changes in the material decreasing hopping distance and decreased electrode separation.^[10,37] We note that the point at which the drop occurs is highly dependent on the shell’s graphene volume%, meaning the former would appear to be the dominant mechanism. Fitting Equation 2 to the data in Figure 2D, we see that G had a peak value of ~ 18.6 for capsules with a shell loading of ≈ 9.3 volume%, after which values decreased with increasing loading level to ≈ 5.5 at ≈ 22.2 volume%. Extrapolated values for W increased from ≈ 0.025 to ≈ 0.040 for a similar volume% range in Figure S11 (Supporting Information). Hence, the materials here are ideal for wearable electronic applications where high sensitivity at low strain limits are highly desirable, like measuring heart function. Furthermore, in the same figure, we confirm W and yield strain’s relationship, with both datasets overlaying each other closely.

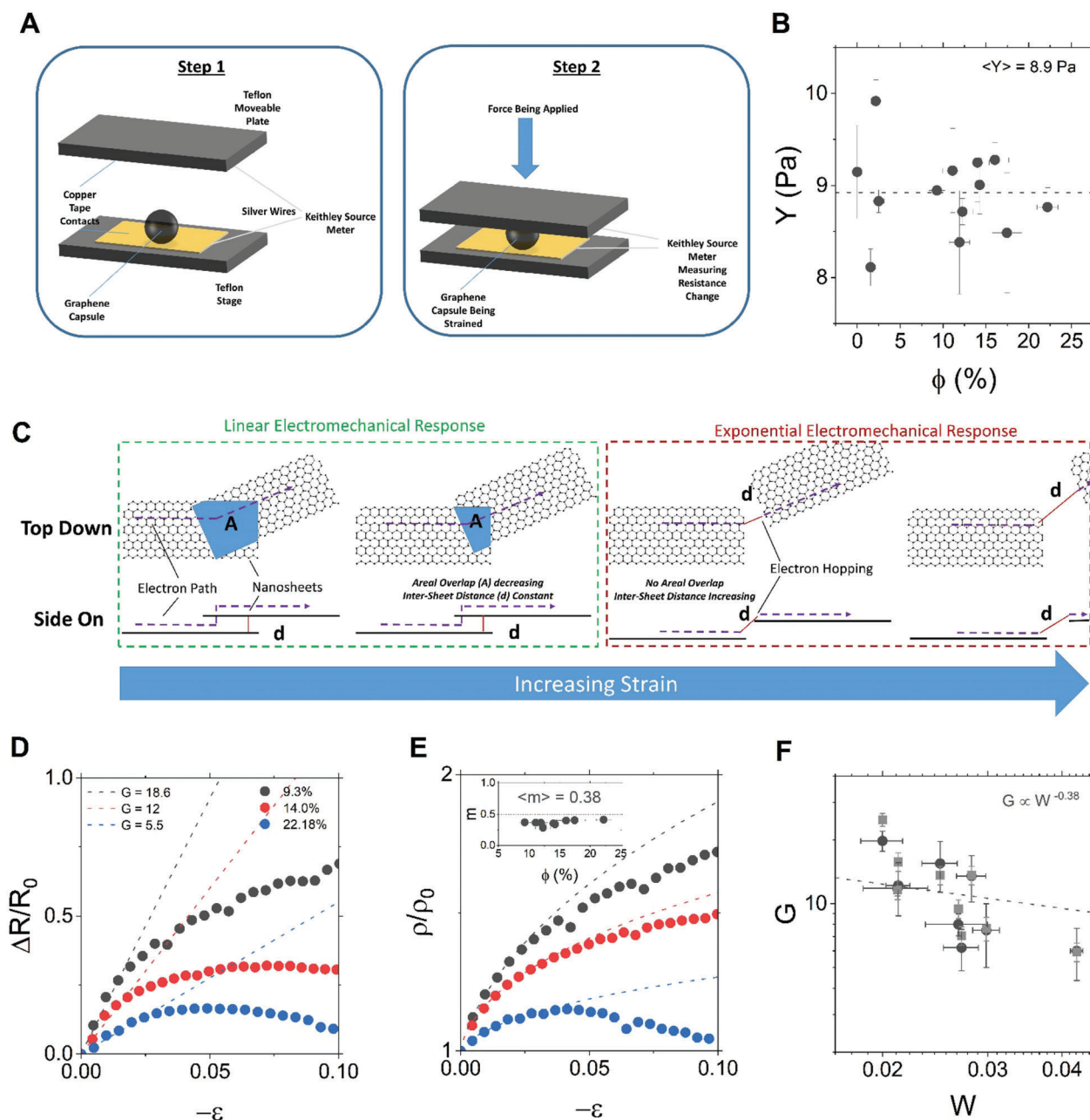


Figure 2. Capsule loading level dependent mechanical and electromechanical properties. A) Scheme presenting the experimental setup used to test both the mechanical and electromechanical properties of the graphene capsules. In step 1, the capsule is loaded between the test plates. Step 2, force is applied to a capsule sandwiched between two test plates that have copper tape contacts attach to their inside face. B) Young's module of capsules versus shell graphene volume%. Dashed line represents the mean modulus value of 8.9 Pa. C) Scheme showing the proposed electromechanical mechanism which is based on areal overlap and inter-sheet distances controlling linear and exponential response in a nanocomposite, respectively. D) Fractional resistance change plotted against compressive strain. Dashed lines are a fit for Equation 3. Inset, extrapolated values for Kraus constant versus shell graphene volume% where solid line represent $m = 0.5$ F) Measured and calculated (from Equation 4) G plotted against W scaled with $m \approx 0.38$ (Equation 5).

2.3. A General Electromechanical Model

Previously, Kraus demonstrated a model which described the number of filler network connections changing as a function of strain in a polymer composite.^[38] Alternatively, we present a modified version of this model to create a description of how a

nanocomposite's electrical properties, in the form of resistivity (ρ), in a high viscosity sample changes as a function of strain. Applying our experimental observation that W is directly related

to yield strain:

$$\rho \approx \rho_0 \left[1 + \left(\frac{\epsilon}{W} \right)^{2m} \right]^{n_e} \quad (3)$$

Where ρ_0 is the zero-strain resistivity, m the Kraus constant which has a universal value of 0.5 for ideal systems and n_e is a system specific scaling exponent believed to be related to filler alignment. For Figure 2E and Figure S12 (Supporting Information), Equation 3 suitably overlaid ρ/ρ_0 versus $-\epsilon$ data up to each datasets respective W value, with values for m and n_e found via the fitting (Figure S13, Supporting Information). For the datasets, a constant value of $m \approx 0.38 \pm 0.08$ was found for all graphene loadings (inset Figure 2E). This value was within error of the universal value and consistent with experimental values which report m to vary between 0.3 to 0.6.^[20,38,39]

Through the Kraus model, a system constant (C_0) associated with the ratio of bond reformation and breaking in a filler network with strain can be related to W and m by $C_0 \approx W^{2m}$ (see Figure S14, Supporting Information).^[39] When assuming that m should ideally be ≈ 0.5 , the following expression can be derived from Equation 3 and the equation for C_0 , which predicted G values for a given system based solely on the ratio of n_e to W .^[3,20]

$$G \approx 2 + \frac{n_e}{W} \quad (4)$$

In Figure 2F, both measured and calculated (via Equation 4) values of G plotted as a function of W were seen to overlay one another closely, confirming the predictive nature of our model. Furthermore, in the same figure, we see that both G values scaled with W according to a power-law described by:

$$G \propto W^{-m} \quad (5)$$

Predictably the scaling exponent for the data was ≈ 0.38 , the mean value of m for the dataset. We validated the scaling predicted in Equation 5 by fitting literary data with Equation 3, where we find our model to be in good agreement with the plots (Figures S15–S17, Supporting Information). For literary data, G scaled with W according to each respective system's extrapolated m value, thus confirming the scaling in Equation 5. In fact, we see that our findings here described a previous universal scaling between G and W ,^[3,35,40] where $G \propto W^{-0.5}$. Here, we confirm that the universal scaling exponent is in fact the Kraus constant, m . This observed universal scaling can be viewed as a reflection of G being inversely proportional to W in Equation 4 when m is ≈ 0.5 (i.e., W^{-2m}).

Fundamentally, our model shows that when G is large, intrinsically W will always be small. But most powerfully, our model explains why this is the case. In terms of engineering sensing materials for epidermal applications, the relationship in Equation 5 primarily affects the expectations of nanocomposites usage. The research focus of the field suggestibly should be narrowed into two categories:

- 1) high accuracy, low strain measurements (i.e., high G , low W)
- 2) low accuracy, high strain measurements (i.e., low G , high W).

2.4. Geometry (In)Dependent Properties

From our electromechanical model, it outlines a blueprint for attaining very large G values through maximizing the value of n_e . As previously noted, we believe n_e to be a metric for filler alignment in a nanocomposite. We set out to control n_e 's value by altering the diameter of 9.3volume% capsules between 1.44 and 4.5 mm (Figure 3A) while also keeping the concentration of polymer constant. We note that through this method, shell thickness (Figure 3B; Figure S19, Supporting Information) and zero-strain resistance (R_0) (Figure 3C) were invariant when $D \leq 2.5$ mm. Values for these properties scattered $\approx 650 \mu\text{m}$ and $\approx 2.6 \text{ M}\Omega$ respectively in this diameter range. However, above a critical diameter of 2.5 mm, both properties scaled with D according to a power-law exponent of -2 , with t and R_0 decreasing to minimum values of $\approx 300 \mu\text{m}$ and $1 \text{ M}\Omega$, respectively, when $D \approx 4.5$ mm. For mechanical properties we note a similar scaling exponent when modeling the data using standard mechanical, Hertzian, and core confinement models (see Section S10 and Figures S19–S22, Supporting Information). To understand the scalings seen in t and R_0 , we developed a simple model to describe the electrical properties of our capsules when describing their structure as having internal and external diameters, D_1 and D_2 respectively (Figure 3D; Figure S23, Supporting Information). Here, R_0 can be written in terms of capsule geometry as:

$$R_0 = \frac{\rho}{\pi} \left(\frac{t}{D_1 D_2} \right) \quad (6)$$

When the ratio $t/D_2 D_1 \rightarrow 1$ (i.e., $D \leq 2.5$ mm), geometry independent R_0 was expected (Figure S24, Supporting Information). However, for $D > 2.5$ mm, t became small, capsule volume (V) thus scaled as $V \approx \pi D^2 t$ (i.e., $t \propto D^{-2}$) and Equation 6 became:

$$R_0 \approx \frac{\rho t}{\pi D^2} \quad (7)$$

We believed that $t \propto R_0$ in Equation 7 implied that nanosheet alignment was occurring in the shells as t became small, resulting in transversal confinement of the network and a subsequent decrease in R_0 (Figure 3E). Being able to finely tune alignment in a nanocomposite would be highly beneficial, as G in the past has been reported to greatly increase with filler alignment.^[32] Here, we investigated geometry controlled alignment through polarized Raman spectroscopy (Figure S25, Supporting Information).^[41] Looking at the normalized G-band intensity for a thin shelled and presumably highly aligned $D \approx 4.5$ mm sample, we observed intensity to rapidly increase as a function of beam angle. In Figure 3F, intensity was noted to be at a minimum for a beam angle of 0° (perpendicular to shell) and a maximum at 90° (parallel), with this behavior suggestive of the shell containing an anisotropic graphene network aligned in plane with the shell's surface.^[42] In Figure 3G, normalized G-band intensities at 90° for $D \leq 2.5$ mm samples was noted to be invariant. Thus, implying that the network of nanosheets for this diameter range were isotropic.^[42] However, for $D > 2.5$ mm, intensity scaled as D^2 , indicative of anisotropic filler network behavior increasing with diminishing t .

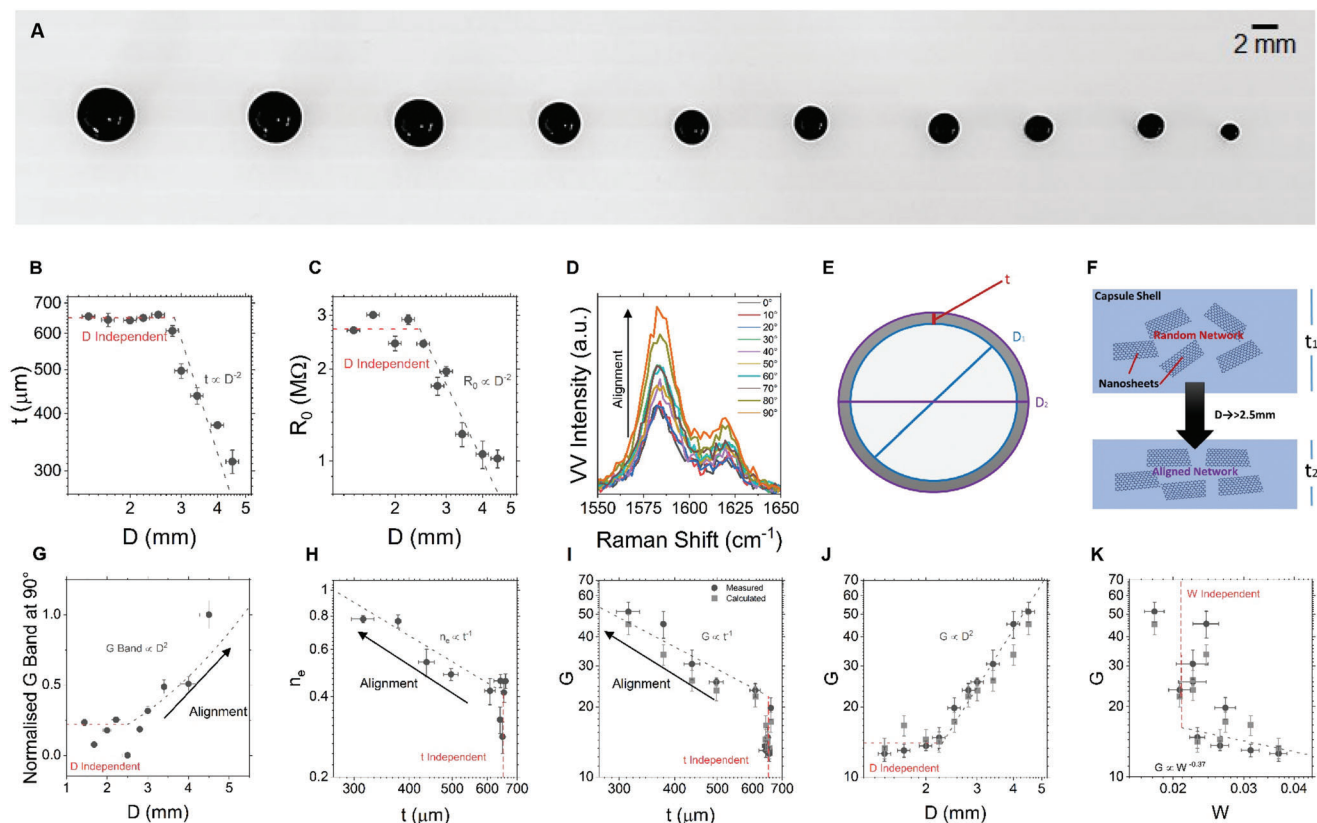


Figure 3. Capsule properties as a function of diameter. A) Photograph of capsule size range (4.5 mm to 1.44 mm left to right). B) Shell thickness scaled as a function of diameter accordingly with volumetric changes in the capsule structure above 2.5 mm. C) Zero-strain resistance versus diameter scaled as Equation 7 above 2.5 mm. D) Polarized Raman spectra of 4.5 mm capsule, G-band intensity shown as a function of beam angle. E) Diagram of a graphene capsule describing how the geometric shape can be described more completely via a shell thickness t , internal diameter D_1 and an external diameter D_2 . F) Scheme showing proposed mechanism describing how nanosheet networks become confined in a capsules shell when t decreases (i.e. $t_1 > t_2$) above the critical diameter of $D > 2.5$ mm, resulting in increased network alignment. G) Normalized G-band intensity at beam angle of 90° versus diameter scaled as D^2 above 2.5 mm. H, I) n_e and G (measured and calculated via Equation 4) varied with thickness-controlled alignment, following a power-law exponent of -1 when $D > 2.5$ mm. J) Similarly, when $D > 2.5$ mm, $G \propto D^2$ (per Equation 9). However, G was invariant when $D \leq 2.5$ mm, a reflection of previous findings. K) Alignment resulted in G and W becoming decoupled for $D > 2.5$ mm and scaled as Equation 5 with exponent of ≈ 0.37 (similar to Figure 2F) below the critical diameter.

The electromechanical response of the capsules as a function of diameter followed a similar trend as before (Figure S26, Supporting Information), allowing for Equation 2 to be fitted to the datasets at low strain to extrapolate values of G and W (Figure S27, Supporting Information). Furthermore, fitting Equation 3 to ρ/ρ_0 versus $-\epsilon$ plots (Figure S28, Supporting Information) again facilitated the quoting of n_e and m values (Figure S29, Supporting Information). In Figure 3H, n_e was found to have a constant value of ≈ 0.4 when t was invariant (i.e., $D \leq 2.5$ mm). However, when $D > 2.5$ mm, n_e scaled as $1/t$, increasing to ≈ 0.8 . This is consistent with polarized Raman data, thus confirming that n_e is a universal metric for filler alignment. Similarly, in Figure 3I, G (measured and calculated) showed an identical data trend due as $G \propto n_e$ from Equation 4, with a constant value of ≈ 14 noted in the t invariant region and values increasing to ≈ 60 as t decreased, further validating both the expression and alignments positive effect on G .

To now understand how the diameter of the capsules directly affect electromechanical sensitivity, we can combine Equations 2

and 6 to yield:

$$G = \frac{\Delta R \cdot \pi D_1 D_2}{\rho t \epsilon} \quad (8)$$

Expectedly, from Equation 8, G was invariant with geometry when the ratio $D_2 D_1 / t \rightarrow 1$ for $D \leq 2.5$ mm (Figure S30, Supporting Information). However, when t was small, Equation 8 became:

$$G = \frac{\Delta R \cdot \pi D^2}{\rho t \epsilon} \quad (9)$$

In Figure 3J, G scaled as D^2 above the critical diameter (i.e., 2.5 mm) as per Equation 9. Plotting G as a function of W in Figure 3K, G scaled according to W^{-m} , where $m \approx 0.37 \pm 0.05$ when $D \leq 2.5$ mm. This phenomenon in W when $D \leq 2.5$ mm can be attributed to the areal overlap of the nanosheets being artificially increased due to longitudinal confinement brought about by decreasing capsule diameter when volume% and t was constant (Figure S31, Supporting Information). However, we saw in

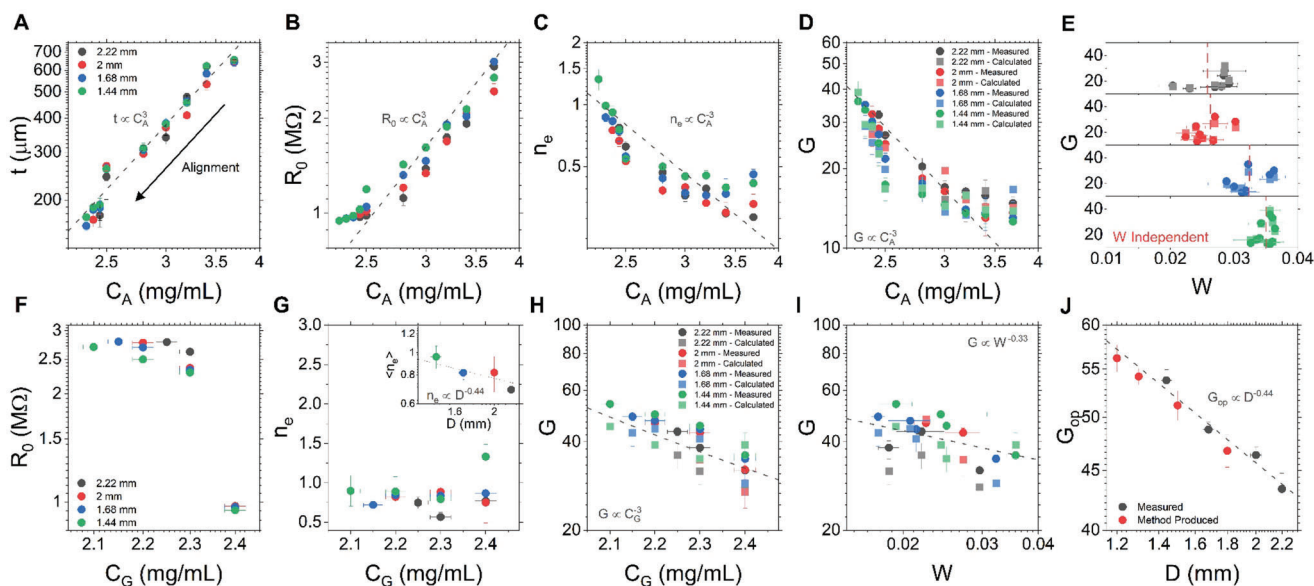


Figure 4. Optimization of $D < 2.5$ mm capsules using general model. A,B) Shell thickness and zero-strain resistance scale with alginate concentration according to similar power-law exponent of 3 due to alignment effects (C&D) n_e and G (measured and calculated, Equation 4) also followed similar inverse power-law scaling with alginate-controlled alignment as per Figure 2F,G and Figure S54 (Supporting Information). E) W was found to again be invariant with alignment-controlled G (Equation 4), similar to Figure 2I. Dashed red lines are mean values of W . F) Zero-strain resistance as a function of graphene concentration. G) n_e versus graphene concentration. Inset, mean n_e across graphene concentrations against diameter followed a power-law exponent of -0.44 . H) Measured and calculated G versus graphene concentration scaled similarly as 3C and D. I) G via graphene variations versus W , scaling exponent $m \approx 0.33$ (Equation 5). J) G from optimized and method produced capsules via Figures S55 and S74 (Supporting Information) scalings with D according to power-law with same exponent noted in 3G inset, -0.44 .

Figure 2F that W also increased with volume%, which could lead to the assumption that network connectivity plays a significant role. But for the sample range here, R_0 was decoupled from diameter and held at a constant value, while W independently varied. Ultimately, we conclude the quality of connections in a filler network does not influence the magnitude of W . Furthermore, Figure 3K also showed that G and W became decoupled when alignment increased for $D > 2.5$ mm. Decisively, W relies only on filler areal overlap (Figure S32, Supporting Information), while G can increase independently with geometry-controlled alignment through n_e .

2.5. Controlling and Optimizing Electromechanical Performance

Using our previous findings and general model, we investigated how the electromechanical performance of the geometry independent diameter range of $D < 2.5$ mm can be manipulated. Our goal was to develop a method to scale capsule diameter towards being micron-sized to facilitate the creation of discrete electronic devices. By reducing the alginate concentration (C_A) for the capsule samples with $D < 2.5$ mm (i.e., 1.44, 1.68, 2, and 2.22 mm), we were able to force t to scale with C_A according to a power-law with an exponent of 3 (Figure 4A; Figure S33–S36, Supporting Information). Values of t were noted to decrease from ≈ 650 μm to ≈ 150 μm when C_A went from ≈ 3.7 to 2.4 mg mL^{-1} respectively. As previously observed in Figure 3, decreasing t was conducive of transversal confinement of the filler network. As such, R_0 for a similar range of C_A values in Figure 4B also scaled as C_A^3 (i.e., $t \propto R_0$ per Equation 7), decreasing from ≈ 3 to ≈ 1

$\text{M}\Omega$. From recording (Figures S37–S40, Supporting Information) and modelling (Figures S41–S45, Supporting Information) electromechanical data, in Figure 4C, the alignment metric n_e scaled as C_A^{-3} from ≈ 1 to ≈ 0.4 , with the $n_e \propto 1/t$ behavior previously associated with geometry-controlled alignment of fillers again observed. In Figure 4D, measured and calculated G increased from ≈ 13 to ≈ 40 according to a power-law exponent of -3 , similar to the scalings noted in Figure 4A–C when taking proportionalities into account (Figure S46, Supporting Information). Furthermore, in Figure 4E, W was reconfirmed to be invariant with alignment for each diameter size. Values for W scaled with D , similar to our observation in Figure 3K, steadily increasing from ≈ 0.025 for $D \approx 2.2$ mm to ≈ 0.035 for $D \approx 1.68$ mm.

Interestingly, with capsule diameter now decoupled from alignment (i.e. n_e here being controlled only by C_A), mechanical properties were observed to be invariant with alignment for each diameter size (see Section S17 and Figures S47–S54, Supporting Information). This is most advantageous for applications, as increases in Young's modulus with nanosheet alignment lead to signal dampening when applying nanocomposites.^[43] For each diameter size we noted a minimum C_A value, whereby below this value capsules would no longer form. Essentially, our model acted as a blueprint which enabled the identification of a scaling law between the critical C_A concentration and diameter to enable the optimization of G for capsules of increasingly smaller size (Figure S55, Supporting Information).

As nanocomposites generally display a peak sensitivity near the percolation threshold, we needed to compensate for alignment increasing the connectivity of the nanosheet network to further optimize performance. This was done by decreasing the

starting graphene concentration (C_G) so as $\phi \rightarrow \phi_c$ to further optimize G . C_G was decreased from ≈ 2.4 to ≈ 2.1 mg mL⁻¹ for each capsule size (i.e., 1.44, 1.68, 2, and 2.22 mm) produced using their respective critical C_A amount. This reduction in graphene amount resulted in a sharp increase in R_0 from ≈ 1 to ≈ 2.9 M Ω as C_G was reduced (Figure 4F). Looking at the mechanical properties of the capsules, we again find them to be invariant with graphene loading (Figures S56–S63, Supporting Information) and data between diameters to scale as D^{-2} (Figure S64, Supporting Information). From examining (Figures S65–S68, Supporting Information) and fitting (Figures S69–S73, Supporting Information) electromechanical response, in Figure 4G, n_e also marginally increased from ≈ 0.7 to ≈ 1 with decreasing C_G due to natural alignment changes in the network with loading level.^[41] However, plotting mean n_e (i.e., $\langle n_e \rangle$) versus D (inset), a more apparent power-law scaling with exponent of -0.44 was observed. Expectedly, G scaled as C_G^{-3} in Figure 4H, increasing from ≈ 40 to ≈ 55 , with the scaling exponent's magnitude being the same as Figure 4A–D. This strong proportionality between parameters reconfirms the robust connection between G and alignment through n_e in Equation 4. In Figure 4I, G versus W scaled with an exponent of $m \sim 0.33 \pm 0.09$ in accordance with Equation 6, with the value for m being similar to those seen in Figures 2F and 3K. Similar to C_A , each diameter size had a critical C_G value whereby below this value a sample was no longer electrically conducting (i.e., below ϕ_c). This again enabled the development of a scaling law to describe how the critical C_G value scaled with diameter when C_A was minimized in order to further optimize G (Figure S74, Supporting Information). In Figure 4J, optimized values for G (G_{op}) were plotted alongside G_{op} values measured from unexplored capsule diameters generated using our C_A and C_G scaling law method (Figure S75, Supporting Information). We found that both measured and method produced (via C_A and C_G scaling laws) G_{op} values scaled with D according to a power-law fit of exponent -0.44 , the same exponent seen in Figure 4G's inset. Essentially, G_{op} increased due to our method projecting improved alignment and decreased network connections as diameter diminished.

2.6. Graphene Microcapsule Networks

We devised a soft-landing production method (Figure 5A) based on spraying a graphene/alginate solution through a syringe with needles of different gauge (Figures S76 and S77, Supporting Information) to create highly uniform (Figure S78, Supporting Information) capsule size distributions between $D \sim 100$ μ m and $D \sim 1200$ μ m (Figure S79, Supporting Information) at a record rate of >100 samples per second. Using a mesh-based cascade size exclusion method (Figures S80–S84, Supporting Information) and the 34-gauge needle size range (i.e., yielded smallest capsule sizes), materials were easily fractionalized into quantized size distributions (Figure 5B; Figure S85, Supporting Information) of uniform microcapsules (Figure S86, Supporting Information). For this size range specifically, $C_A \approx 1.84$ mg mL⁻¹ and $C_G \approx 1.61$ mg mL⁻¹. These different size fractions were drop-casted on Ecoflex substrates, after which they were encapsulated by a second Ecoflex layer to form our electronic skin heterostructure which was ~ 1 mm in total thickness when applying our small-

est microcapsule size fraction (Figure 5C). Due to the unique structure of our electronic skins, the Ecoflex layers and silver wire leads were fully recyclable, with both materials easily recovered by simply peeling the two Ecoflex layers apart and cleaning the two surfaces of microcapsules and silver paint with warm water. The networks that formed the basis of our electronic skins were quasi-2D in nature (Figure 5D), meaning the network was planar and one capsule thick. In Figure 5E, as a function of network size (from 1 mm² to 25 mm²), values of G_{op} for a $\langle D \rangle \approx 650$ μ m electronic skin scattered around the theoretical value for a single 650 μ m microcapsule predicted by $G_{op} \propto D^{-0.44}$. This implied that in theory our electronic skins could be scaled toward single capsule devices for high areal resolution electronics. Like random, planar piezoresistive networks of printed graphene^[44] which contain gaps, voids and network sections that are disconnected or do not contribute to electromechanical response; the authors report here that when consistent experimental procedures are adhered to, the randomness of microcapsules in the quasi-2D networks does not lead to performance discrepancies between electronic skin samples. When making the electronics skins from size fractions with decreasing $\langle D \rangle$ values (Figure 5F), G_{op} values were found to rapidly increase (Figure 5G; Figure S87, Supporting Information). In fact, we found that all G_{op} values from the study sat on a master plot (Figure 5H) described by the same power-law exponent of -0.44 , previously observed in Figure 4G, J. For electronic skins based off microcapsules with $\langle D \rangle \approx 290$ μ m, we report an impressive peak value of $G_{op} \approx 108$, far above the average of ≈ 40 for a nanocomposite.^[20,45] In comparison to a diverse range of electronic skin devices based on hydrogels ($G \approx 2.6$),^[46] microstructured polymers ($G \approx 7.7$),^[47] electrospun fibers membranes ($G \approx 9$)^[48] and stacked electronic heterostructures ($G \approx 20.8$),^[49] we find our devices to also exceed their contemporaries. Furthermore, our simple electronic skins displayed remarkably robust long-term performance stability, ideal for potential application testing (Figure S88, Supporting Information).

When attaching a $\langle D \rangle \approx 290$ μ m microcapsule electronic skin to different locations on the body, we demonstrated the device as a highly sensitive diagnostic tool; measuring muscular movement, breathing and pulse (Figure 6A–C respectively) all in real-time. We noted that for muscular movements in Figure 6A, our electronic skins were able to record motion associated with the clenching of the hand into a fist at fast and slow rates. Similarly, for breathing, whereby the electronic skin was attached to the skin above the ribcage, in Figure 6B, a clear distinction between inhaled and exhaled were observed. For pulse measurements in Figure 6C, where the electronic skin was held to the carotid artery in the neck, pulse as a function of time was measured. Due to the high sensitivity associated with our electronics skins, the characteristic systolic and diastolic peaks, as well as the dicrotic notch were observed in our measurements.

Blood pressure is the quintessential measurement of good health in a person. Here, we take our graphene capsule electronic skins and demonstrate the state-of-the-art health application potential of these materials by measuring blood pressure in real-time. Blood pressure is commonly characterized by the systolic and diastolic pressures associated with the pressure in the arteries when a person's heart beats and the ambient pressure in the arteries between beats, respectively.^[50] For a healthy person, blood pressure is said to be 120/80 mmHg.^[51] Though as a stan-

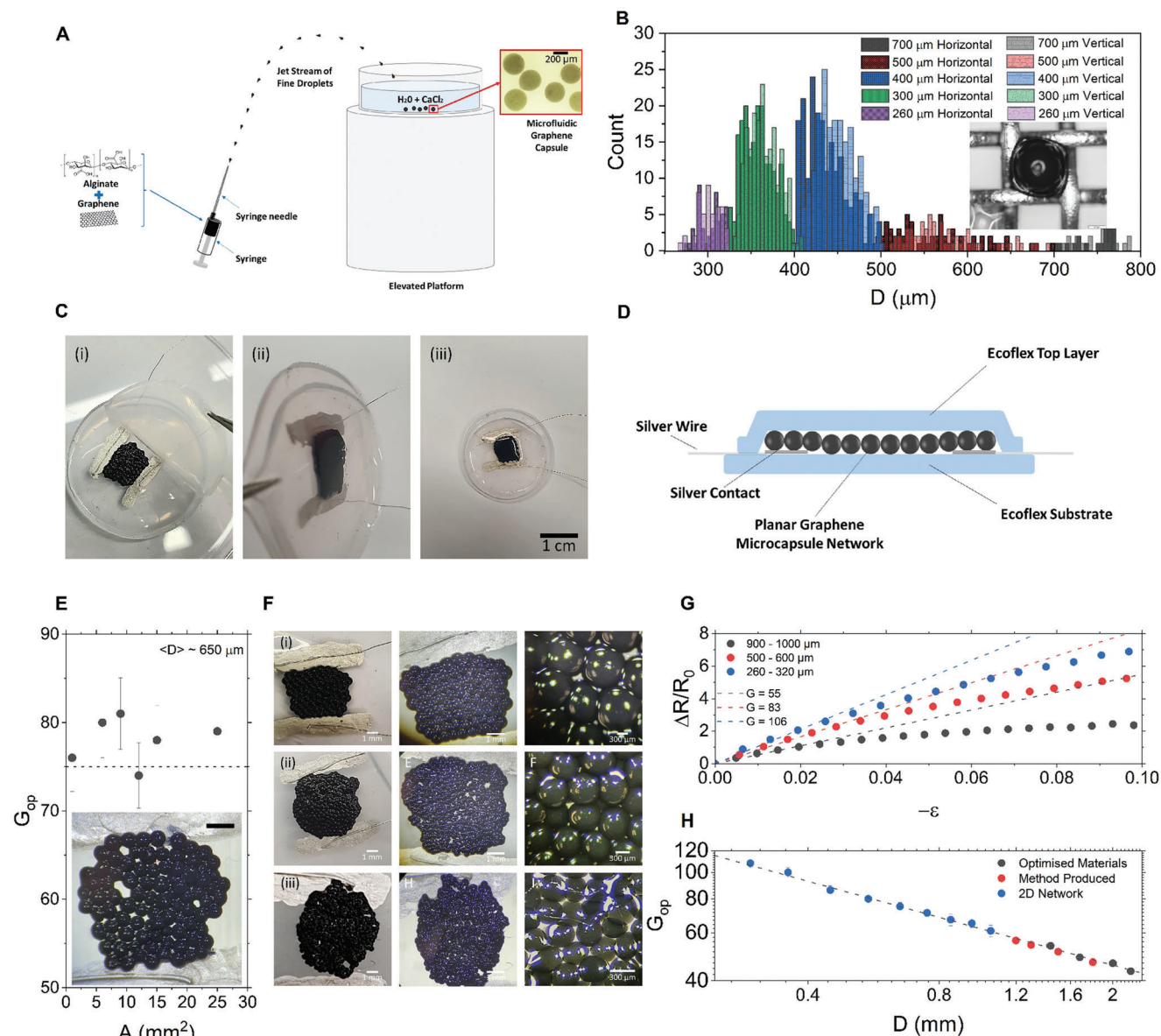


Figure 5. Electronic skins based on quasi-2D microcapsule networks. A) Scheme of graphene microcapsule production through a soft-landing method. B) Mesh-based cascade size exclusion diameter fractions of microcapsules. Inset, optical image of graphene microcapsule trapped by 500 μm steel wire mesh. C) Construction of $\langle D \rangle \approx 850 \mu\text{m}$ electronic. i) Capsules are deposited onto a layer of Ecoflex between silver paint contacts and silver wire leads previously adhered to the surface. ii) A thin layer of Ecoflex is then placed across the surface of the sample, fully encapsulating the capsules. iii) A completed electronic skin. D) Scheme showing the cross-section of an assembled electronic skin device. E) Optimized gauge factor for $\langle D \rangle \approx 650 \mu\text{m}$ electronic skin was invariant with quasi-2D network areal size. Dashed line is the predicted optimized gauge factor of a single $\langle D \rangle \approx 650 \mu\text{m}$ capsule. Inset is an optical image of a $\langle D \rangle \approx 650 \mu\text{m}$ microcapsule quasi-2D network ($A \approx 5 \text{ mm}^2$) between to silver electrodes on a Ecoflex substrate, scale bar equivalent to $\approx 1 \text{ mm}$. F) Optical image collage of different size fraction microcapsule networks: i) 800–900 μm , ii) 600–700 μm , iii) 260–320 μm . G) Electromechanical response of quasi-2D networks as a function of mean microcapsule diameter making up the network. H) Master plot of optimized gauge factor for all system types in the study. Dashed line represents scaling previously noted in Figure 4G,J.

standard, healthy blood pressure is described as a range of pressures as depending on age and physical ability there can be broad variations in expected values.

With respect to the measurement of pulse, both the systolic and diastolic pressures can be observed.^[52] In Figure S89 (Supporting Information), the systolic pressure would be related to the peak height of the waveform (R_{peak}) and the diastolic associ-

ated with the baseline minimum (R_{baseline}). Thus, from the measurement of pulse, the difference between the systolic and diastolic pressures can be easily extrapolated to determine blood pressure^[53] if the pulse measurement taken via the electromechanical response of our capsules was calibrated. For normal blood pressure, the difference between systolic and diastolic pressures would be $\approx 40 \text{ mmHg}$.^[53] Though once again, there is a

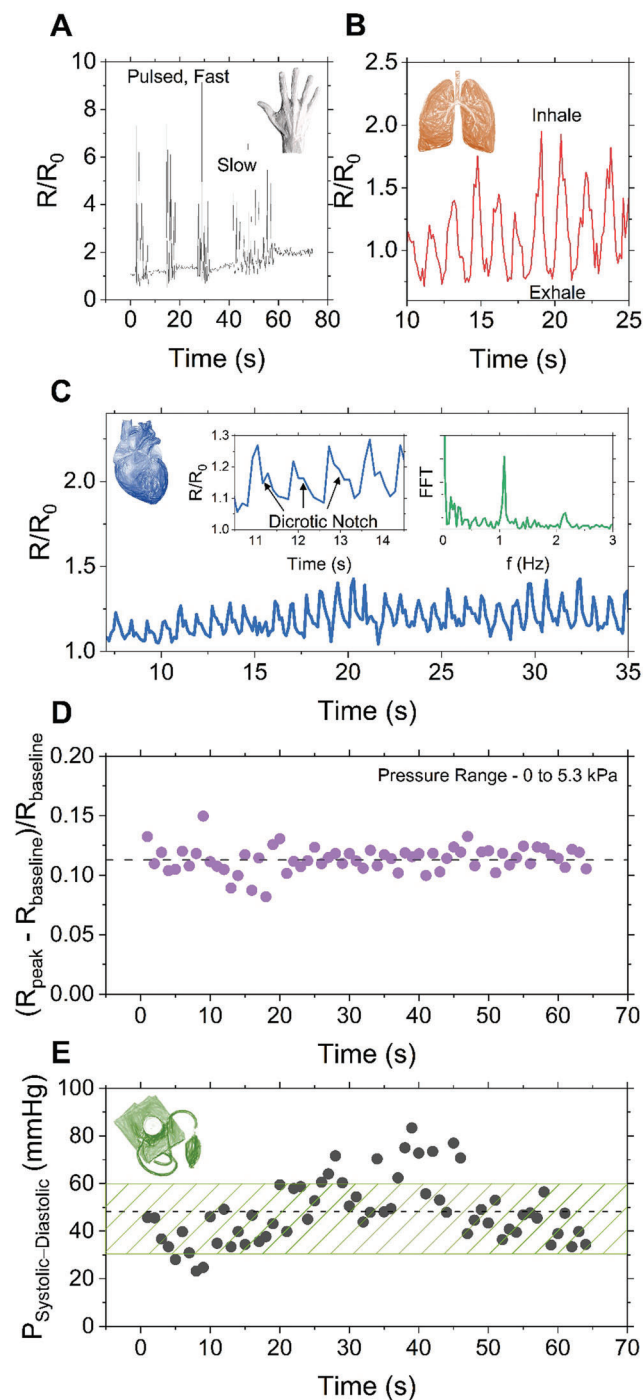


Figure 6. Sensing applications of microcapsule electronic skins. Application of $\langle D \rangle \approx 290 \mu\text{m}$ electronic skin for A) muscular hand movement, B) breathing and, C) pulse measurements. Insets in (C) are a zoomed in look at characteristic pulse waveforms with dicrotic notch (lefthand side) and a FFT showing a normal rate of $\approx 1.1 \text{ Hz}$ respectively (righthand side). D) Fraction resistance $[(R_{\text{peak}} - R_{\text{baseline}})/R_{\text{baseline}}]$ values extrapolated from response peaks in Figure S91 (Supporting Information) show a steady response, with a mean value of ≈ 0.113 (dashed line) found for the calibration constant. E) Blood pressure as a function of time extrapolated through our calibration method. Green zone signifies healthy value range and the dashed line the measured mean of $\approx 48 \text{ mmHg}$.

standard range associated with what value can be defined as being healthy. This is generally between 30 and 60 mmHg.^[53–55]

To calibrate our electronic skins, we took a 270–300 μm size fraction device and tested it in a modified version of our electromechanical tester (Figure S90, Supporting Information). In this setup, a 6.5 mm diameter wire (simulating the dimensions of the carotid artery in the neck) was repeatedly pressed into our electronic skin at a rate of 1.1 Hz (pulse rate of our wearer) over a range of 0 to 5.3 kPa (equivalent to 40 mmHg, a healthy blood pressure). During this cyclic testing, the electromechanical response of the electronic skin was measured. In Figure 5D; Figure S91 (Supporting Information), the response of the electronic skin is shown to be quite uniform with respect to cycle number, with no signs of signal hysteresis. All values for electromechanical response were found to scatter around a mean value of $(R_{\text{peak}} - R_{\text{baseline}})/R_{\text{baseline}} = 0.113 \pm 0.001$ (dashed line). We note that for the composite material g-putty, which had a similar gauge factor in compression ($G \approx 110$) and was also calibrated for blood pressure, reported a similar calibration constant of ≈ 0.1 .^[20] We believe that the matching of calibration constants strongly upholds our calibration methodology. Using the calibration constant and the calculations described in Section S26 and Figures S89–S92 (Supporting Information), in Figure 6D, our electronic skin was shown to accurately measure blood pressure as a function of time. We report here a healthy mean value of $48.222 \pm 1.628 \text{ mmHg}$, with the standard error of our measurement being within the tolerable error limit of $\pm 10 \text{ mmHg}$ required for applied clinical use.^[56]

3. Conclusion

We have demonstrated that seaweed capsules with a graphene additive display a high level of property tunability. Specifically, basic nanocomposite properties associated with mechanical, electrical, and electromechanical properties could be decoupled for in-depth analysis. This facilitated the creation of a general electromechanical model that could be applied to understand and optimize our material's performances to create electronic skin devices for a range of bodily sensing applications.

4. Experimental Section

Graphene Production: A 5 mg mL⁻¹ stock solution of sodium cholate (Sigma Aldrich BioXtra, $\geq 99\%$) was prepared by mixing sodium cholate powder in deionized water at 40 °C for 2 h. A graphene dispersion was prepared by adding graphite flakes (Sigma Aldrich 332 416) to the sodium cholate solution at 100 mg mL⁻¹. The mixture was tip sonicated (Sonics Vibra-cell VCX130) for 5 h at 60% amplitude with a configuration of 6 s on and 2 s off. After sonication, the mixture was centrifuged for 90 min at 1500 rpm and the supernatant decanted. The supernatant was then vacuum filtered onto a nylon filter membrane (pore size of 0.2 microns and 47 mm in diameter), with the filtered material redispersed in the sodium cholate solution to form a 5 mg mL⁻¹ stock solution through bath sonication (Fisher Scientific FB 15051 ultrasonic bath, 30% amplitude for 1 h). Mean lateral length of the nanosheets in the stock solution were measured on a silicon wafer substrate using a Bruker Dimension Icon Atomic Force Microscope.

Capsule Production: The graphene stock solution was diluted to create several dispersions ranging in concentration from 0.1 to 4 mg mL⁻¹.

For each one of these diluted dispersions, sodium alginate (Special Ingredients, Molecular Gastronomy Ingredient) was added at a concentration of 3.7 mg mL^{-1} . To create the macro-sized samples, the method of choice was hand expressing, drop-by-drop, the sodium alginate/graphene dispersion into a curing bath consisting of calcium chloride (0.8 mg mL^{-1} ; IntraLabs, DiHydrate Flakes) dissolved in deionized water using an Eppendorf Research plus Variable Adjustable Volume Pipettes (Single-Channel). Pipette volume for this method was either $10 \mu\text{L}$, $100 \mu\text{L}$, or 1 mL and depended on the target droplet size. Upon contact with the curing bath, the droplet was encapsulated by an outer layer or shell which resulted in the formation of a free-standing, 3D spherical object which was called a capsule. This capsule system consisted of a calcium alginate/graphene hydrogel shell surrounding a liquid graphene dispersion core. Depending on the pipette tip aperture diameter and the amount of sodium alginate/graphene expressed, the diameter of the droplet could be finely controlled. The droplet size directly corresponded to the diameter of the resultant capsule formed, which were generally between ≈ 1.2 and $\approx 4.5 \text{ mm}$ in diameter for this method type. After formation, capsules were removed from the bath and placed in deionized water for storage. The sizes of the capsules formed were measured using a digital micrometer. This process could also be demonstrated to be semi-automated by using a burette suspended above the curing bath. By having the stopcock opened slightly to allow for a constant drop-by-drop extrusion (until the liquid ran out), an increased production rate could be demonstrated. Using a similar methodology, droplet and thus capsule size could be controlled using different aperture sized burettes. The weight percentage of graphene in the shell of each capsule formed was calculated through thermogravimetric analysis (TGA 550-TA Instruments). Using the densities of both graphene and sodium alginate, 2200 and 1600 kg m^{-3} respectively, weight percent was converted to volume percent. The thickness of the hydrogel layer was measured through profilometry (Bruker DektakXT), whereby capsules were burst with a lab blade and rectangular segments cut out and placed on a glass slide for measurement. Raman spectroscopy measurement was carried out using a Renishaw inVia. Differential scanning calorimetry was performed using PerkinElmer DSC 4000.

Microcapsule Production: For micron sized capsules, the sodium alginate/graphene dispersion was loaded into a 5 mL total volume syringe. Depending on the desired capsule distribution size range, flat head needles of gauge 34, 32, 27, and 25 were used to create capsule distributions ranging in diameter from ≈ 100 to $\approx 1200 \mu\text{m}$. As it was sought to produce the smallest possible capsules, the 34 gauge needle was used for the data in Figure 4. Placing the curing bath on an elevated platform (a standing distance of $\approx 45 \text{ cm}$ from the surface of the workbench to the surface of the bath's liquid level) the syringe was held $\approx 40 \text{ cm}$ away from the platform's base. The needle was then pointed upwards at the bath at an angle of ≈ 70 degrees. The entire contents of the syringe were then hand expressed using as much pressure as possible (the user felt resistive counter pressure due to liquid confinement when doing so). The resultant was a jet-stream of droplets exiting the needle tip and travelling upwards in an arc-like path, reaching its apex $\approx 5 \text{ cm}$ above the bath's surface. At the apex, droplet velocity reached zero and the resultant velocity beyond this point associated with the droplet moving toward the bath surface was minimized, facilitating the soft-landing of spherical-like droplets entering the bath. After formation, capsules were removed from the bath and placed in deionized water for storage. Capsule diameter distributions were measured using an Olympus BX53M optical microscope fitted with a 4K digital CCD camera while the capsules were suspended in deionized water.

Microcapsule Size Selection: Using a developed filtration method, which were called mesh-based cascade size exclusion, specific sized capsules could be isolated or removed from the distribution of capsules formed using the soft-landing method. Specifically, for the creation of the electronic skins, capsules $< 320 \mu\text{m}$ in size were most desirable for application due to their predicted state-of-the-art electromechanical performances and their moderate abundance in the distribution. To isolate this diameter fraction, distributions created using the 34-gauge needle were filtered using a stainless-steel woven mesh (Mesh Direct) first with an aperture size of $320 \mu\text{m}$, thus all sizes $> 320 \mu\text{m}$ were excluded from the solution of capsules. This was then followed by filtration with a $260 \mu\text{m}$ mesh, resulting

in all sizes $< 260 \mu\text{m}$ passing through. Thus, capsules with sizes between 260 and $320 \mu\text{m}$ have been isolated. In all cases for the wire mesh filtration, a VWR Analog Rocker 2 Tier (tilt of 0 to 4 degrees and rpm of 30) was used to aid capsule pathing through the mesh.

Electronic Skin Production: Equal volumes of Part A and Part B of Ecoflex 00–30 were mixed, then placed in a vacuum oven under full vacuum for 5 mins to degas. The mixture was then drop casted into glass petri dishes and left to set for 4 h at room temperature to form thin substrate layers of 100 and $500 \mu\text{m}$ in thickness depending on drop cast quantity. Once dried, the Ecoflex layers were removed from the petri dishes with half the quantity of layers acting as a substrate and the other a solid state, self-encapsulating covering layer. For the designated substrate layers ($\approx 500 \mu\text{m}$ in thickness), silver paint contacts with silver wire leads were drawn ($\approx 1 \text{ cm}$ in length) onto the layer ($\approx 6 \text{ mm}$ apart). A solution of size-selected micro-sized capsule were then moved onto the surface of the Ecoflex substrate and using a VWR Analog Rocker 2 Tier (tilt of 0 to 4 degrees and rpm of 30), micro-capsules gradually assessable into an even, tightly packed layer approximately one capsule thick. Excess water was removed using lab roll. The covering layer ($\approx 100 \mu\text{m}$ in thickness) was then placed directly on top of the capsule layer. Owing to the softness and thickness associated with the Ecoflex layers used to construct electronic skins, the top and bottom layers formed an airtight seal around the capsule layer due to an accumulative van der Waals effect between the two flat surfaces. To observe the areal dependence on the electromechanical properties of the capsule layer, electronic skins with layer, contact length and separation of various sizes were produced.

Capsules of known macro-diameter were deformed, and the mechanical properties obtained using a texture analyzer (Stable Micro Systems TA-TXplus). This setup consisted of the capsule being placed on a flat, insulating sample stage and a plate shaped, insulating testing arm applying stress and/or strain to the capsule system. Data was recorded on the computer system paired to the tester. Simultaneously, the electrical properties of the capsules were measured during the same instance. On the faces of the sample stage and the plate, electrically conductive copper tape was attached. When moved into the starting position, the capsule lay in contact between these two copper tape contacts. The copper tape was attached to a Keithley 2614B source meter using silver wire which supplied a current across the sample and measured resistance change as the capsules were deformed by the tester. Electrical data was recorded by the same computer system which was also paired to the source meter. For testing the electromechanical properties of the quasi-2D assembled layers of the micro-sized capsules, the electronic skin was placed onto the sample stage of the mechanical tester and the silver wire leads were attached to the Keithley source meter.

Applications: Bodily sensing applications were performed using an electronic skin make from a capsule size fraction of 260 – $320 \mu\text{m}$. For the muscular movement measurements, the electronic skin was attached directly onto the dorsal surface of the hand below the knuckle of the first and second digit. All the fingers of the hand were then opened and closed (i.e., forming a fist) at different rates, with the electromechanical response of the skin measured simultaneously. For breathing and lung function, the electronic skin was attached to the skin above the sixth and seventh rib of the ribcage. The wearer then breathed at an exaggerated respiration rate to simulate exercise with electromechanical response again measured as a function of time. For pulse, the electronic skin was held up to the carotid artery in the neck of the user. All bodily testing was performed by the author Adel K.A. Aljarid on his own person.

Supporting Information

Supporting Information is available from the Wiley Online Library or from the author.

Acknowledgements

A.K.A.A., C.W., and C.S.B. acknowledge funding from the Saudi Arabian Cultural Bureau and the University of Sussex Strategic Development Fund.

M.D., Y.H., and D.G.P. acknowledge funding support from “Graphene Core 3” GA: 881603 implemented under the EU-Horizon 2020 Research & Innovation Actions (RIA) and supported by EC-financed parts of the Graphene Flagship. D.G.P. also acknowledges support from The Royal Society through RGS\R2\212410.

Conflict of Interest

The authors declare no conflict of interest.

Author Contributions

A.K.A.A. made all nanocomposite samples and performed all geometric, electrical, mechanical and electromechanical measurements; M.D., Y.H., and D.G.P. performed all Raman and DSC measurements; C.W. performed AFM analysis and assisted with video recording; JPS took SEM images; C.S.B. planned all methods and experiments, performed modelling, wrote and revised the manuscript.

Data Availability Statement

The data that support the findings of this study are available from the corresponding author upon reasonable request.

Keywords

electromechanics models, electronic skins, graphene, health sensing, nanocomposites, piezoresistive

Received: April 6, 2023

Revised: May 14, 2023

Published online:

- [16] L.-Q. Tao, K.-N. Zhang, H. Tian, Y. Liu, D.-Y. Wang, Y.-Q. Chen, Y. Yang, T.-L. Ren, *ACS Nano* **2017**, *11*, 8790.
- [17] Z. Yang, Y. Pang, X.-L. Han, Y. Yang, J. Ling, M. Jian, Y. Zhang, Y. Yang, T.-L. Ren, *ACS Nano* **2018**, *12*, 9134.
- [18] Q. Liu, M. Zhang, L. Huang, Y. Li, J. Chen, C. Li, G. Shi, *ACS Nano* **2015**, *9*, 12320.
- [19] R. Zhao, L. Jiang, P. Zhang, D. Li, Z. Guo, L. Hu, *Soft Matter* **2022**, *18*, 1201.
- [20] C. S. Boland, U. Khan, G. Ryan, S. Barwich, R. Charifou, A. Harvey, C. Backes, Z. Li, M. S. Ferreira, M. E. Möbius, R. J. Young, J. N. Coleman, *Science* **2016**, *354*, 1257.
- [21] S.-H. Hwang, et al., *ACS Appl. Nano Mater.* **2018**, *1*, 2836.
- [22] Y. Pang, K. Zhang, Z. Yang, S. Jiang, Z. Ju, Y. Li, X. Wang, D. Wang, M. Jian, Y. Zhang, R. Liang, H. Tian, Y. Yang, T.-L. Ren, *ACS Nano* **2018**, *12*, 2346.
- [1] I. A. Kinloch, J. Suhr, J. Lou, R. J. Young, P. M. Ajayan, *Science* **2018**, *362*, 547.
- [2] D. G. Papageorgiou, I. A. Kinloch, R. J. Young, *Prog. Mater. Sci.* **2017**, *90*, 75.
- [3] C. S. Boland, *ACS Nano* **2019**, *13*, 13627.
- [4] D. G. Papageorgiou, I. A. Kinloch, R. J. Young, *Carbon* **2015**, *95*, 460.
- [5] Y. Lu, M. C. Biswas, Z. Guo, J.-W. Jeon, E. K. Wujcik, *Biosens. Bioelectron.* **2019**, *123*, 167.
- [6] M. A. U. Khalid, S. H. Chang, *Compos. Struct.* **2022**, *284*, 115214.
- [7] B. Dong, et al., *Ind. Eng. Chem. Res.* **2016**, *55*, 4919.
- [8] H. Liu, H. Gao, G. Hu, *Composites, Part B* **2019**, *171*, 138.
- [9] C. S. Boland, U. Khan, C. Backes, A. O’neill, J. Mccauley, S. Duane, R. Shanker, Y. Liu, I. Jurewicz, A. B. Dalton, J. N. Coleman, *ACS Nano* **2014**, *8*, 8819.
- [10] C. S. Boland, U. Khan, M. Binions, S. Barwich, J. B. Boland, D. Weaire, J. N. Coleman, *Nanoscale* **2018**, *10*, 5366.
- [11] Y. Qin, Q. Peng, Y. Ding, Z. Lin, C. Wang, Y. Li, F. Xu, J. Li, Y. Yuan, X. He, Y. Li, *ACS Nano* **2015**, *9*, 8933.
- [12] J. Li, et al., *ACS Appl. Mater. Interfaces* **2016**, *8*, 18954.
- [13] X. Wang, S. Meng, M. Tebyetekerwa, Y. Li, J. Pionteck, B. Sun, Z. Qin, M. Zhu, *Composites, Part A* **2018**, *105*, 291.
- [14] H. Zhai, L. Xu, Z. Liu, L. Jin, Y. Yi, J. Zhang, Y. Fan, D. Cheng, J. Li, X. Liu, Q. Song, P. Yue, Y. Li, *Chem. Eng. J.* **2022**, *439*, 135502.
- [15] H. Lee, M. J. Glasper, X. Li, J. A. Nychka, J. Batcheller, H.-J. Chung, Y. Chen, *J. Mater. Sci.* **2018**, *53*, 9026.

- [23] S. Wu, et al., *ACS Appl. Mater. Interfaces* **2016**, *8*, 24853.
- [24] Q. Liu, J. Chen, Y. Li, G. Shi, *ACS Nano* **2016**, *10*, 7901.
- [25] B. Yin, et al., *ACS Appl. Mater. Interfaces* **2017**, *9*, 32054.
- [26] X. Tao, S. Liao, Y. Wang, *EcoMat* **2021**, *3*, e12083.
- [27] C. Bennacef, S. Desobry-Banon, L. Probst, S. Desobry, *Food Hydrocolloids* **2021**, *118*, 106782.
- [28] Y. Qin, et al., in *Biopolymers for Food Design*, (Eds: A. M. Grumezescu, A. M. Holban), Academic Press, Cambridge, MA **2018**, 409.
- [29] C. Backes, T. M. Higgins, A. Kelly, C. Boland, A. Harvey, D. Hanlon, J. N. Coleman, Guidelines for Exfoliation, Characterization and Processing of Layered Materials Produced by Liquid Exfoliation, *Chem. Mater.* **2017**, *29*, 243.
- [30] U. Khan, A. O'Neill, M. Lotya, S. De, J. N. Coleman, *Small* **2010**, *6*, 864.
- [31] G. T. Grant, E. R. Morris, D. A. Rees, P. J. C. Smith, D. Thom, *FEBS Lett.* **1973**, *32*, 195.
- [32] C. S. Boland, *ACS Appl. Nano Mater.* **2020**, 11240.
- [33] D. Stauffer, A. Aharony, *Introduction To Percolation Theory*, CRC Press, Boca Raton, FL **1994**, p. 205.
- [34] A. J. Marsden, D. G. Papageorgiou, C. Vallés, A. Liscio, V. Palermo, M. A. Bissett, R. J. Young, I. A. Kinloch, *2D Mater.* **2018**, *5*, 032003.
- [35] A. A. K. D. Aljarid, Kevin, C. Wei, J. Salvage, C. S. Boland, *ACS Sustainable Chem. Eng.* **2023**.
- [36] J. G. Simmons, *J. Appl. Phys.* **1963**, *34*, 1793.
- [37] C. S. Boland, et al., *ACS Appl. Mater. Interfaces* **2021**, *13*, 60489.
- [38] G. Kraus, *J Appl Polym Sci Symp* **1984**, 75.
- [39] G. Heinrich, M. Klüppel, in *Filled Elastomers Drug Delivery Systems*, Springer Berlin Heidelberg, Berlin, Heidelberg **2002**, 1-44.
- [40] M. T. Innocent, et al., *ACS Appl. Mater. Interfaces* **2022**.
- [41] Z. Li, R. J. Young, N. R. Wilson, I. A. Kinloch, C. Vallés, Z. Li, *Compos. Sci. Technol.* **2016**, *123*, 125.
- [42] Z. Li, R. J. Young, I. A. Kinloch, N. R. Wilson, A. J. Marsden, A. P. A. Raju, *Carbon* **2015**, *88*, 215.
- [43] C. S. Boland, *ACS Appl. Polym. Mater.* **2020**, *2*, 3474.
- [44] E. Caffrey, et al., *ACS Appl. Mater. Interfaces* **2022**, *14*, 7141.
- [45] D. P. O'driscoll, S. McMahon, J. Garcia, S. Biccai, C. Gabbett, A. G. Kelly, S. Barwich, M. Moebius, C. S. Boland, J. N. Coleman, *Small* **2021**, *17*, 2006542.
- [46] Y. Yu, Y. Feng, F. Liu, H. Wang, H. Yu, K. Dai, G. Zheng, W. Feng, *Small* **2022**, 2204365.
- [47] M. Lei, K. Feng, S. Ding, M. Wang, Z. Dai, R. Liu, Y. Gao, Y. Zhou, Q. Xu, B. Zhou, *ACS Nano* **2022**, *16*, 12620.
- [48] C. Ma, et al., *Adv. Mater. Technol.* **2022**, *7*, 2200106.
- [49] J. Li, et al., *Small Sci.* **2022**, *2*, 2100083.
- [50] CDC. High Blood Pressure Symptoms, Causes, and Problems | cdc.gov. Centers for Disease Control and Prevention. <https://www.cdc.gov/bloodpressure/about.htm> (accessed: May 2021).
- [51] NHS. High blood pressure (hypertension). nhs.uk <https://www.nhs.uk/conditions/high-blood-pressure-hypertension/> (accessed: April 2023).
- [52] M. F. O'rourke, A. Pauca, X.-J. Jiang, *Br. J. Clin. Pharmacol.* **2001**, *51*, 507.
- [53] T. D. Homan, S. Bordes, E. Cichowski, in *StatPearls*, StatPearls Publishing, Treasure Island, FL **2022**.
- [54] Mayo Clinic, Pulse Pressure: An Indicator of Heart Health? Mayo Clinic, Rochester, MN **2022**.
- [55] A. M. Dart, B. A. Kingwell, *J. Am. Coll. Cardiol.* **2001**, *37*, 975.
- [56] G. S. Stergiou, B. Alpert, S. Mieke, R. Asmar, N. Atkins, S. Eckert, G. Frick, B. Friedman, T. Graßl, T. Ichikawa, J. P. Ioannidis, P. Lacy, R. McManus, A. Murray, M. Myers, P. Palatini, G. Parati, D. Quinn, J. Sarkis, A. Shennan, T. Usuda, J. Wang, C. O. Wu, E. O'Brien, *Hypertension* **2018**, *71*, 368.